Research Article

Submilliwatt, widely tunable coherent microcomb generation with feedback-free operation

Haowen Shu,[a,†] **Lin Chang,**[b,†,‡] **Chenghao Lao,**[c,†] **Bitao Shen,**[a,†] **Weiqiang Xie,**[b,§] **Xuguang Zhang,**[a] **Ming Jin,**[a] **Yuansheng Tao,**[a] **Ruixuan Chen,**[a] **Zihan Tao,**[a] **Huajin Chang,**[a] **Shaohua Yu,**[a,d] **Qifan Yang,**[c,e] **Xingjun Wang** ⓘ,[a,d,e,*] **and John E. Bowers** ⓘ[b,*]

[a]Peking University, School of Electronics, State Key Laboratory of Advanced Optical Communication Systems and Networks, Beijing, China
[b]University of California, Santa Barbara, Department of Electrical and Computer Engineering, Santa Barbara, California, United States
[c]Peking University, School of Physics, State Key Laboratory for Artificial Microstructure and Mesoscopic Physics, Beijing, China
[d]Peng Cheng Laboratory, Shenzhen, China
[e]Peking University, Frontiers Science Center for Nano-Optoelectronics, Beijing, China

Abstract. Microcombs are revolutionizing optoelectronics by providing parallel, mutually coherent wavelength channels for time-frequency metrology and information processing. To implement this essential function in integrated photonic systems, it is desirable to drive microcombs directly with an on-chip laser in a simple and flexible way. However, two major difficulties have prevented this goal: (1) generating mode-locked comb states usually requires a significant amount of pump power and (2) the requirement to align laser and resonator frequency significantly complicates operation and limits the tunability of the comb lines. Here, we address these problems by using microresonators on an AlGaAs on-insulator platform to generate dark-pulse microcombs. This highly nonlinear platform dramatically relaxes fabrication requirements and leads to a record-low pump power of <1 mW for coherent comb generation. Dark-pulse microcombs facilitated by thermally controlled avoided mode crossings are accessed by direct distributed feedback laser pumping. Without any feedback or control circuitries, the comb shows good coherence and stability. With around 150 mW on-chip power, this approach also leads to an unprecedentedly wide tuning range of over one free spectral range (97.5 GHz). Our work provides a route to realize power-efficient, simple, and reconfigurable microcombs that can be seamlessly integrated with a wide range of photonic systems.

Keywords: dark-pulse microcomb; direct pumping scheme; widely tunable source.

*Address all correspondence to Xingjun Wang, xjwang@pku.edu.cn; John E. Bowers, bowers@ece.ucsb.edu

†These authors contributed equally to this work.
‡Present Address: Peking University, School of Electronics, State Key Laboratory of Advanced Optical Communication Systems and Networks, Beijing, China
§Present address: Shanghai Jiao Tong University, Department of Electronic Engineering, State Key Laboratory of Advanced Optical Communication Systems and Networks, Shanghai, China

1 Introduction

Microcombs have witnessed great success in the last decade.[1–7] Due to the important advantages of generating coherent, equidistant optical frequency lines in a scalable way,[8,9] they provide a promising solution for a wide range of applications, such as communications, sensing, computation, spectroscopy,[10,11] optical clocks,[12] and frequency synthesis.[13] To facilitate their use in these systems, a major goal in the development of microcombs throughout their history has been to generate coherent comb states efficiently, simply, and with wide tuning range. Although remarkable advances have been made toward this goal in both

fabrication[4,14-20] and operating principle,[3,21,22] so far there is still no approach that can firmly provide all of these properties. This obstacle prevented the spread and further commercialization of microcomb technologies, but has now been solved.

One essential problem is the high pump power requirement. In particular, for miniaturization and ultimately high-volume production of integrated systems, microcombs need to be directly pumped by an on-chip laser, whose pump power is usually in the tens of milliwatts range. To generate combs efficiently in this power regime, tremendous efforts have been spent on the improvement of microresonator quality factors (Q) over the last decade by fine-tuning fabrication recipes. So far, the Si$_3$N$_4$ platform leads in this regard, due to its extraordinary Q, now up to tens of millions for thick Si$_3$N$_4$ microresonators[23] and hundreds of millions for thin ones.[4] The required pump power for coherent comb states (bright solitons or dark pulses) can be reduced to below 20 mW, which can be reached by an on-chip distributed feedback (DFB) laser or Fabry–Perot (FP) laser diode.[1-5] However, such advances in resonator Q rely on many extra fabrication procedures, including chemical-mechanical polishing and high temperature annealing. These procedures add cost to the fabrication.

Another key challenge comes from the operation side. Nowadays, the mainstream work of microcombs leverages dissipative Kerr solitons (so-called bright solitons) for coherent comb generation. Since these states exist at the red detuning side of the resonance of the cavity,[24] they are sometimes inaccessible due to the intracavity thermal dynamics and therefore require special tricks to align the pump laser and the resonances in soliton formation. The most commonly used strategies are currently active capture techniques and delicate tuning.[21,25] These approaches require benchtop laser sources and complex control protocols, which are not suitable for integrated photonic systems. Recent demonstrations of direct pumping based on self-injection locking have enabled turnkey soliton operation by directly coupling an on-chip laser into a microresonator, which gets rid of all the tuning procedures and greatly simplifies the microcomb generation scheme.[2,3,5] However, such coupling relies on either hybrid or heterogeneous integration, which demands significant effort in process development and has not yet been integrated into existing photonic infrastructures. Importantly, all of the approaches discussed above need feedback, either optical or electrical, to lock the laser frequency within the access window of a coherent state that is usually quite narrow (usually within 1 GHz for bright soliton and megahertz level for injection locking). Hence, they all suffer from a limited modulation range of comb lines. These drawbacks affect the performance in many essential applications such as lidar[26] and spectroscopy.[27]

In this work, we address this long-standing problem by generating dark-pulse microcombs on a highly nonlinear photonic platform, aluminum gallium arsenide-on-insulator (AlGaAsOI). Due to the giant third-order nonlinear coefficient ($n_2 \approx 1.7 \times 10^{-17}$ m^2 W^{-1} at C-band),[28] AlGaAsOI microresonators support coherent comb generation with an unprecedented low pump level of 930 μW with moderate Q value, which significantly relaxes the fabrication requirements, as well as enabling direct pumping of AlGaAsOI dark pulse by a commercial DFB laser diode. By thermally controlling the avoided-mode-crossings (AMXs) in AlGaAsOI microresonators with normal dispersion, dark-pulse microcombs can be readily generated without electronic feedback control. The strong thermal nonlinearity of AlGaAs also facilitates the stable operation of microcombs

by creating an ultrawide window up to 97.5 GHz under a pump power of ~150 mW, which is over an entire free spectral range (FSR), for the desired coherent state. This appealing feature delivers a record high chirping range for all comb lines with good uniformity. The phase and intensity noise of a free-running comb across the entire C-band is verified, which shows short-term linewidth of several kilohertz and the average relative intensity noise (RIN) down to −135 dB Hz^{-1}. This approach provides an appealing microcomb solution for a wide range of system-level optoelectronic applications and holds great potential for fully integrated photonic systems in the future.

2 Results

2.1 Dark Pulse in an AlGaAsOI Microresonator

The AlGaAsOI microresonator used in this work is shown in Fig. 1(a). The epitaxial AlGaAs is transferred onto a silicon substrate with a 3-μm thick thermal silica layer via a wafer bonding process. With optimal fabrication process,[29,30] intrinsic Q factors over 2 million are achieved [see Fig. 1(b)], corresponding to waveguide propagation loss of 0.3 dB/cm. Figure 1(c) shows the cross section of the waveguide, where the thickness of the AlGaAs core is 400 nm. With this geometry, the TE0 mode in a 1 μm width waveguide is anticipated to feature normal dispersion around 1550 nm based on numerical simulation [see Fig. 1(d)]. Experimental measurement of the TE0 mode family dispersion from 1510 to 1630 nm is plotted in Fig. 1(e), which explicitly shows normal dispersion. Hybridization of TE0 modes and neighboring modes is observed at certain wavelengths, and the resulting AMX expels the resonances from the parabolic fitting curve. The hybrid mode, which is redshifted from its original position, induces local anomalous dispersion and initiates parametric oscillation when it is sufficiently pumped.[31-34] The dispersion spectrum measured at 23.1°C shows that a hybrid mode is redshifted by 0.32 GHz due to AMX [see Fig. 1(f)].

The AMX strength is critical to the formation of the dark-pulse microcomb. In the AlGaAsOI platform, it can be changed by thermally tuning the frequency shift difference between the coupling mode pair. The temperature of the microresonator is controlled using a thermoelectric cooler underneath the chip. Due to the distinct mode confinement of neighboring modes, their frequency difference could change accordingly as a function of temperature. Figure 1(g) shows the normalized transmission of the hybrid modes near $\mu = 0$ measured at different temperatures. It is noted that the relative frequency of the left branch is shifted toward the red side as the temperature decreases, and also the mode transmission of the right branch changes sharply, showing the AMX thermal tuning process.[35]

The microresonator is first pumped by an external cavity diode laser for microcomb generation. The waveguide dimension is 1 μm × 400 nm. With 5 mW optical power launched into the bus waveguide, frequency comb formation is observed when the laser is manually tuned into a mode, as shown in Fig. 2(a). The transmission of comb power features four steps associated with different states of microcombs.[36] Unlike the case of bright solitons in microresonators with anomalous dispersion,[24,37-40] abrupt change of intracavity power is not as significant here. Figure 2(b) compares the optical spectra of the microcombs at different stages, whose spans are broadened as the detuning between the laser and mode increases. The spacing between adjacent comb lines is two FSRs of the microresonator. At
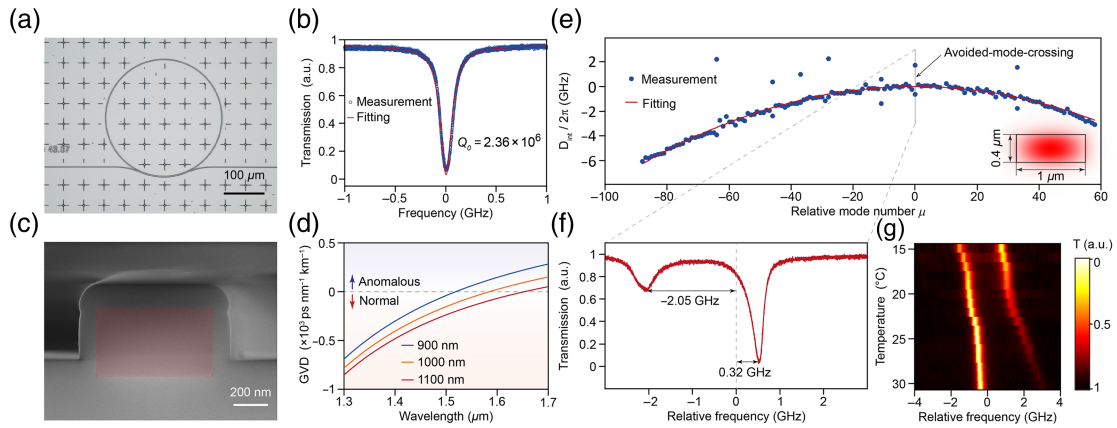
Fig. 1 Resonator characterization. (a) Top-view photograph of the AlGaAsOI microresonator. The radius of the microresonator is 144 μm, corresponding to 91 GHz FSR. Scale bar: 100 μm. (b) Normalized transmission spectrum of a typical resonance at 1552 nm. Lorentzian fitting reveals intrinsic Q factors about 2.36×10^6. (c) Scanning-electron-microscopy image showing the cross section of the microresonator. The AlGaAs core is highlighted in red, and silica forms the substrate and cladding. Scale bar: 200 nm. (d) Calculated dispersion of the TE0 mode in AlGaAsOI microresonators with respect to the width of the core. The thickness of the core is set as 400 nm. The inset shows the corresponding TE0 mode profile. (e) Measured TE0 mode family dispersion. $D_{\text{int}} = \omega_\mu - \omega_o - D_1 \mu = D_2 \mu^2/2 + \mathcal{O}(\mu^3)$, where ω_μ is the resonant frequency of the μth mode. The index of the mode that is pumped is set to 0, and D_1 is the FSR at pump wavelength. Parabolic fitting (red) shows $D_2/2\pi = -1.63$ MHz. (f) Zoom-in spectrum of the doublet resonances at $\mu = 0$ indicated in (e). The frequency is plotted relative to the fitting curve. (g) Pseudo-color plot of the relative frequency shifting of the coupled mode pairs from the ideal resonant frequency without the AMX effect, as a function of temperature.
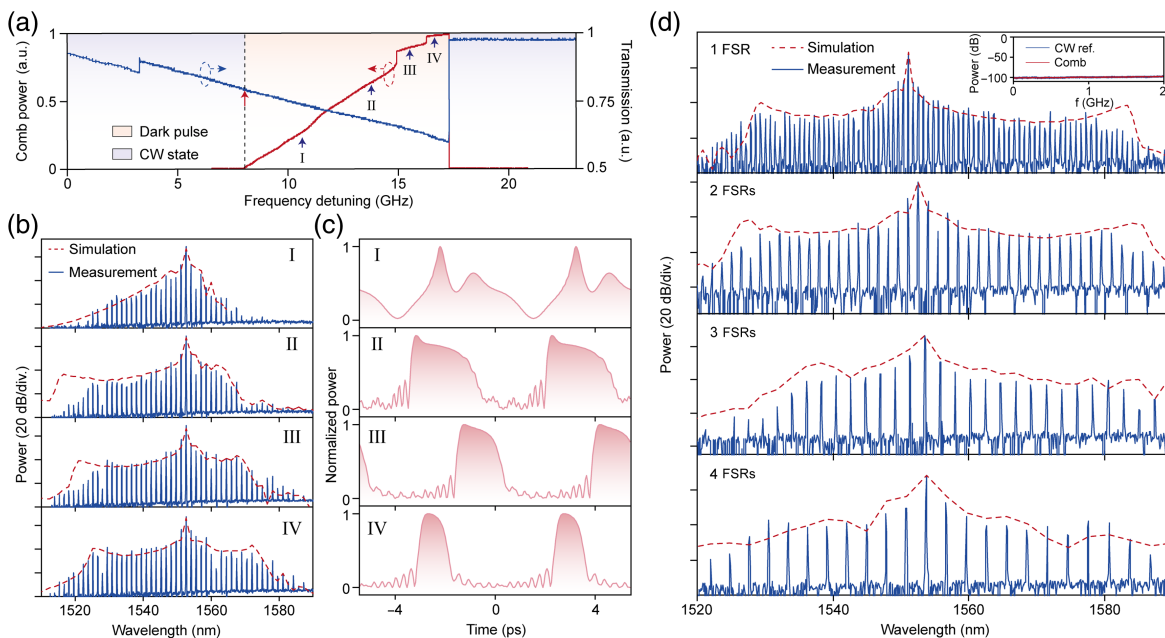

Fig. 2 Dynamics of mode-locked microcombs. (a) Normalized transmitted total power (blue) and comb power (red). The laser is scanned from the blue side to the red side of the mode. Blue and red shadings indicate CW state and microcomb state, respectively. (b) Typical optical spectra of microcombs at different stages as indicated in (a). Red dashed lines denote the simulated spectral envelope. (c) Simulated intracavity waveforms corresponding to the spectra in (b). (d) Optical spectra of microcombs with spacing from 1 to 4 FSRs (top to bottom). Inset: intensity noise of the 1-FSR microcomb (resolution bandwidth: 100 kHz). The noise floor of the measurement system is also plotted for comparison.

stages III and IV, a pair of flat wings are formed on both sides of the pump, which is a signature feature of dark pulses in microresonators.[31] The asymmetry of the spectra results from AMX,[36] which is further confirmed using numerical simulations based on coupled Lugiato–Lefever equations (see Methods and Supplementary Note II in Supplemental Material). The simulated temporal waveforms of the microcombs are plotted in Fig. 2(c). It is noted that the intracavity waveforms could evolve into bright pulses when the detuning is sufficiently large, which agrees well with previous reports.[4,34,36]

Microcombs with perfect multiple-FSR spacing exhibit enhanced power per comb line.[41–43] By adjusting the temperature and pump wavelength, microcombs with varying FSRs are generated, whose optical spectra are shown in Fig. 2(d). The microcomb with a single FSR spacing is photodetected and sent into an electrical spectrum analyzer (ESA). The measured intensity noise of the entire microcomb coincides with the measurement floor, which confirms the mode-locking nature of the microcomb. The remarkable operability of multi-FSR dark pulses

may enjoy great potential at tunable radio-frequency filter[44] and terahertz carrier generation.[45]

2.2 Direct Pumping of Coherent Microcombs

A critical step toward an integrated laser-microcomb source is the realization of a mode-locked microcomb pumped by an on-chip laser, which requires both high efficiency for comb generation and simple operation strategies. In addition to the recently demonstrated laser-soliton microcomb based on injection locking, the dark-pulse comb in AlGaAsOI microresonator gives another solution.[29,46] In our experiment, microcomb generation is still feasible when the pump power is reduced to the submilliwatt-level ($<930~\mu W$), featuring nearly 40 spectral lines spanning the entire C band [see Fig. 3(b)]. The operation power is much smaller than previously reported coherent comb results. At such low power level, a single DFB can drive potentially tens of microcombs, which is invaluable in applications such as communications or dual-comb spectroscopy.
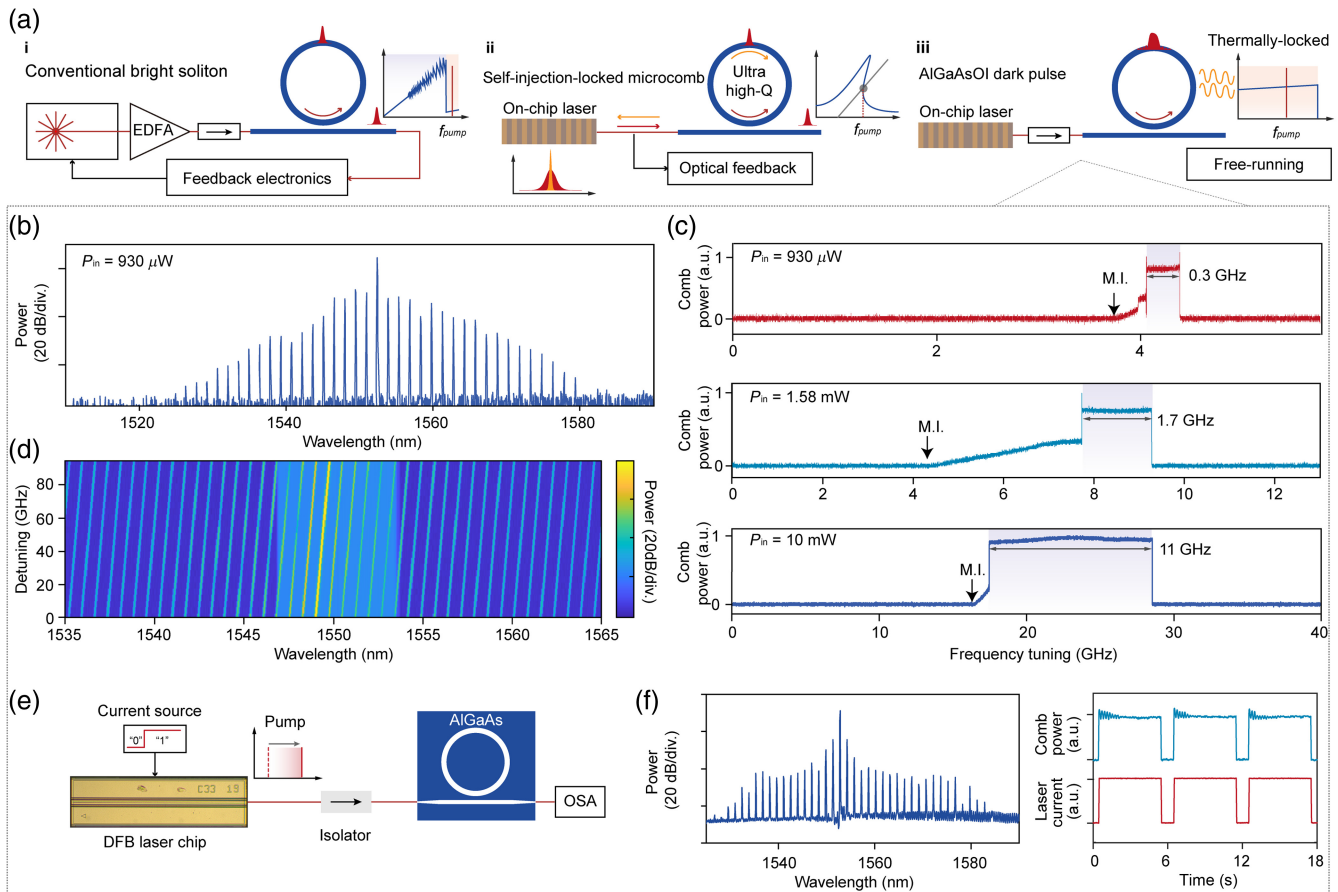

Fig. 3 Power-efficient mode-locked Kerr comb generation. (a) Schematics of different microcomb generation schemes. (b) Comb spectrum at the flat step [shading area in upper panel (c)] under the on-chip pump power of $<930~\mu W$. (c) Measured comb power with respect to the frequency tuning. As the increasing of the pump power, the comb existence area could be extended from 0.3 GHz (upper panel) to 1.7 GHz (mid-panel) and then 11 GHz (lower panel). (d) Wide tuning of the dark-pulse microcomb for 97.5 GHz, which is over an entire FSR. (e) Experimental setup of an on-chip semiconductor laser pumped scheme and (f) comb spectrum. The right panel exhibits that dark-pulse spectrum can be repeatedly accessed with the laser current switched on and off, showing the "turnkey" behavior. All the spectra are of 2-FSR ($\sim$180 GHz) frequency spacing. OSA, optical spectrum analyzer.

In general, a clean "step" of the comb power transmission usually indicates an accessing range of mode-locked comb with small power deviation. For the dark-pulse state, these steps are significantly longer than those of bright solitons due to the thermal stability at blue detuning. And this nature can be further enhanced on AlGaAsOI due to the strong Kerr and thermo-optic effects, which significantly extend the thermal triangle of the response of the cavity. The transmission comb power under different pump powers is recorded in Fig. 3(c), where the "step length" gets extended as the increasing of pump power. With only 1.58 mW of on-chip power, the step size we got has already been around that in bright soliton generation under several hundreds of milliwatts of pump power.[26] At 10 mW, it exhibits an 11 GHz soliton plateau. With ∼150 mW on-chip power, the

existence range of the dark-pulse microcomb could be further extended to 97.5 GHz, which indicates the frequency tuning of microcomb could cover a full FSR range (91 GHz), as shown in Fig. 3(d). Such a long existence range ensures resilience to frequency vibration of the pump laser, particularly for the on-chip lasers whose stability is much worse than external cavity-based narrow linewidth lasers. As a result, this scheme gets rid of the need of any kind of feedback to lock the laser onto the cavity [see Fig. 3(a)]. For proof of concept, we choose a commercial DFB laser with ∼100 kHz linewidth to drive the microresonator, which is coupled to the bus waveguide via a lensed fiber, as shown in Fig. 3(e). An optical isolator is inserted between the laser and the microresonator to reject backreflected signals. The optical spectrum of the 2-FSR-spaced microcomb
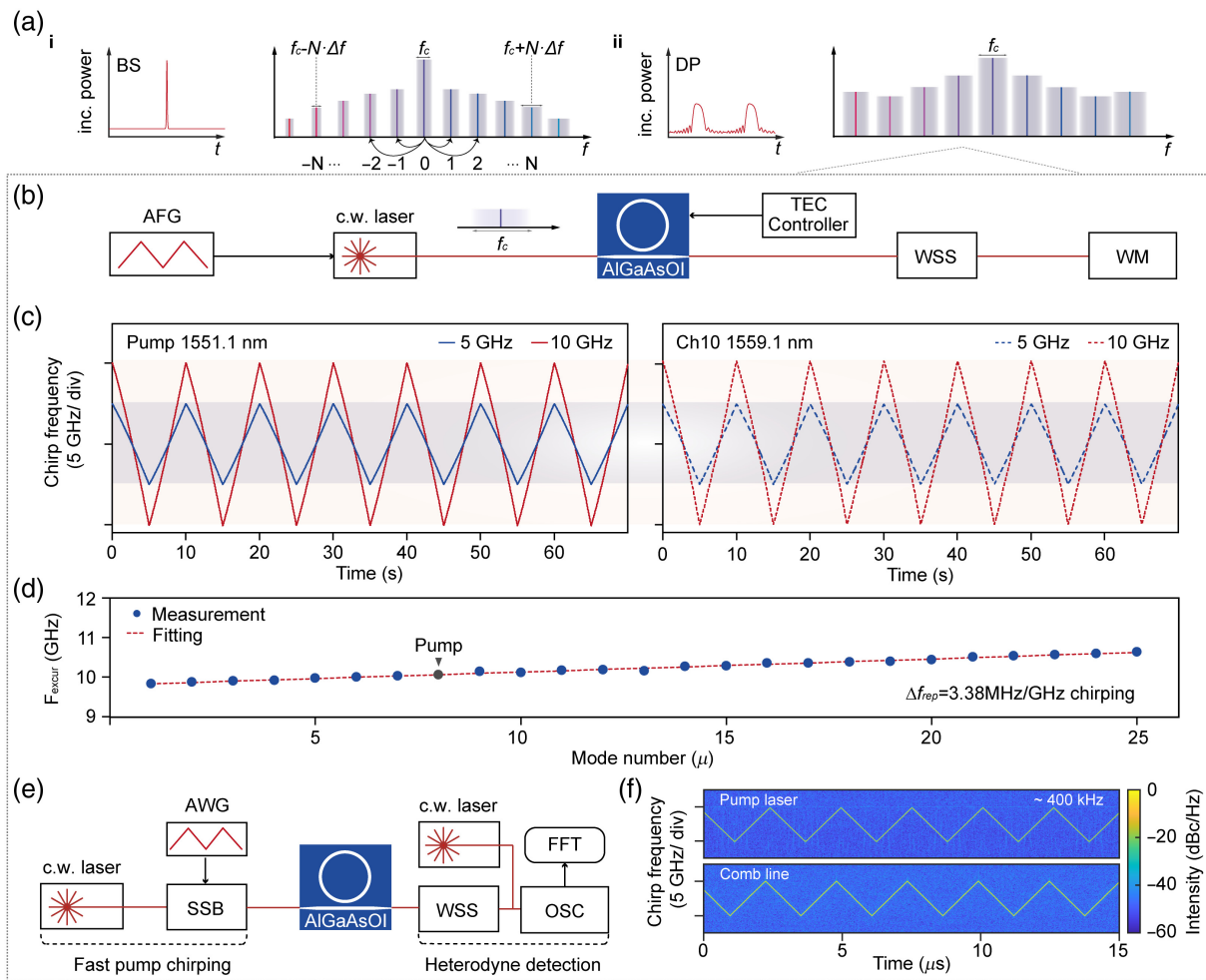

Fig. 4 Widely tunable frequency-chirped microcomb. (a) Both (i) bright soliton and (ii) dark pulse could act as a parallel frequency chirping source, in which the frequency modulation of the pump laser is transduced to each comb line. The stimulated Raman effects and higher-order dispersion would result in wavelength-dependent chirping copies, which could be mitigated in the efficient dark-pulse scheme with relatively low intracavity power. (b) Experimental setup of the parallel chirping source. WSS, wavelength-selective switch; WM, wavelength meter. (c) Measured time-frequency maps of the pump line (left panel) and the channel-10 sideband (right panel), with the pump laser chirping at 5 GHz (blue) and 10 GHz (red), respectively. (d) Frequency excursion of each channel at 10 GHz frequency chirping. (e) Experimental setup of the fast frequency modulation. An SSB modulator is employed as the chirping pump. The modulated comb lines are then charaterized by a heterodyne measurement. SSB, single-sideband modulator; OSC, oscilloscope. (f) Time-frequency maps of 5-GHz chirping pump and a comb line with modulation frequency of 400 kHz.

is plotted in Fig. 3(f). This configuration, compared to injection locking, does not require a specialized chip-to-chip packaging or heterogeneous laser integration but can be easily achieved via the current standard fiber-to-chip packaging process in the integrated photonic industry. Therefore, it can be seamlessly implemented in a wide range of existing photonic systems.

2.3 Widely Tunable Massively Parallel Source

The large step and feedback-free nature offers great frequency chirping capability (see Fig. 4) to this microcomb generation scheme. This is of great importance in many essential applications such as lidar, as the chirping range of the frequency combs is inversely proportional to the fundamental ranging resolution in frequency-modulated continuous-wave (FMCW) scheme.[26,47,48] Figure 4(b) shows the setup to characterize frequency chirping, with details described in Appendix B. As a proof-of-concept demonstration, a triangular frequency modulation scan (5 and 10 GHz) is directly applied to the pump laser acting as an FMCW source [see left panel of Fig. 4(c)]. When the comb operates within the dark-pulse step, the modulated frequency can be transduced to all comb teeth, resulting in a 30-channel parallel FMCW source with >10 GHz frequency excursion bandwidth [see right panel of Fig. 4(c) and Supplementary Note III in the

Supplemental Material]. Such frequency chirping range corresponds to a nearly subcentimeter-level ranging resolution, which is almost 1 order of magnitude better than the previous microcomb-based parallel ranging result.[26]

The repetition frequency shift induced by the stimulated Raman effect[49] and higher-order dispersion[50,51] is a problem in bright soliton comb during the frequency chirping. It causes inconsistencies of the chirping range over different comb lines [see Fig. 4(a)]. Those effects, though still leading to channel-dependent frequency excursion in the dark-pulse regime, can be greatly alleviated in our approach due to the low pump power and large duty cycle of the dark pulse circulating in the cavity, which causes lower peak power. The channel-dependent frequency excursion of each mode is depicted in Fig. 4(d), showing a repetition rate mismatch of only 3.38 MHz per gigahertz of laser tuning, about four times smaller than that in the previous result. Such consistency results in more uniform measurement errors among channels, improving the overall ranging resolution. Moreover, fast microcomb chirping is characterized, as shown in Fig. 4(e), where the pump frequency tuning is applied by a carrier-suppressed single-sideband (SSB) modulator with a 400 kHz modulation frequency. Figure 4(f) depicts the time-frequency map of one chirping comb line, which is highly consistent with the pump laser both in modulation frequency and
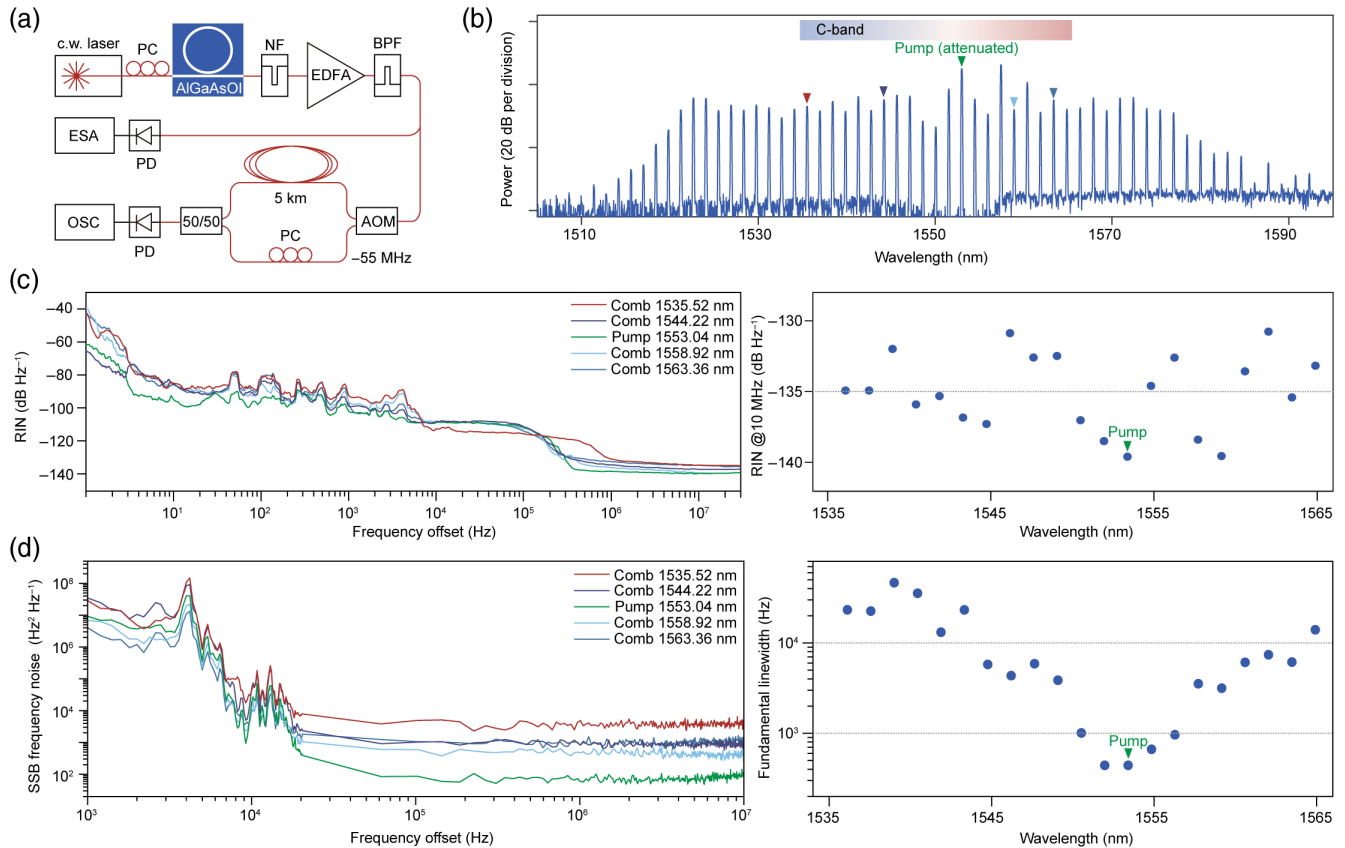

Fig. 5 Coherence of mode-locked frequency comb. (a) Experimental setup. PC, polarization controller; NF, notch filter; EDFA, erbium-doped fiber amplifier; BPF, bandpass filter; AOM, acousto-optic modulator; PD, photodetector; ESA, electric spectrum analyzer; OSC, oscilloscope. (b) Optical spectra of dark-pulse comb after NF. The range of telecommunication C-band is also indicated. (c) Left panel: measured RIN of comb teeth indicated in (b). Right panel: RIN at 10 MHz offset frequencies of all comb teeth within C-band. (d) Left panel: measured SSB frequency noise of comb teeth indicated in (b). Right panel: fundamental linewidth of all comb teeth within C-band.

linearity. The 5 GHz chirping bandwidth here, mainly limited by the working range of the commercial SSB modulator, could get much higher when a more delicate bias control and sideband power equalization are implemented.

2.4 Coherence and Stability of Free-Running Microcomb

The stability and coherence of microcombs are essential in almost all applications. Previously, all these characterizations of microcombs were under certain locking schemes. Here, for the first time, we measure the RIN, phase noise, and long-term stability for a free-running dark-pulse microcomb. The experimental setup of noise evaluation is illustrated in Fig. 5(a); more details are found in Appendix A. The measured 2-FSR microcomb whose optical spectrum shown in Fig. 5(b) spans over 80 nm and features a relatively flat envelope within the telecommunication C-band. RIN measurements of the comb teeth are plotted in Fig. 5(c). At low offset frequencies, the noise is primarily induced by thermal and mechanical instability and by the optical amplifier. For offset frequencies >1 MHz, the RIN maintains constant; the flatline value indicates the intrinsic noise characteristics of the microcomb and is of interest to applications such as data links. The intrinsic RINs of comb lines within the C-band are measured and are all below -130 dB Hz^{-1}, with a few approaching -140 dB Hz^{-1}.

The frequency noise of the comb lines is shown in Fig. 5(d), which converges to white noise above 20 kHz offset frequencies. The fundamental linewidth of the pump is about 400 Hz.

Decoherence of comb lines is observed as their linewidth increases quadratically with their spectral separation from the pump, which can be attributed to the instability of the repetition rate due to the free-running operation mode. The linewidth performance cannot be comparable to that in the injection-locking scheme; nonetheless, the derived fundamental linewidth of the comb lines within C-band is still at the level of a few kilohertz, which is suitable for coherent communications, high-precision sensing, and metrology.

3 Discussion

A comparison of different integrated nonlinear platforms for coherent microcomb generation is shown in Table 1. In this work, the pump power used is the lowest number required for coherent microcomb generation. Also, an ultrawide 97.5 GHz tuning range is achieved in the microcomb with 91 GHz FSR. This is the only type of coherent microcomb, as far as we know, that could cover the entire FSR without any complicated feedback operation.

Although the laser is free-running, the stability of phase and amplitude of the comb lines is sufficient to incorporate complex signal processing and transmission schemes. Meanwhile, the microcomb exhibits robustness and operation simplicity without relying on any feedback. These invaluable properties are very same as the soliton crystals hold,[41] which works at an anomalous dispersion regime, and have already been applied to a series of practical applications.[63–65] The maximum power conversion efficiency we achieved is around 15%, which is more than an

Table 1 Comparison of coherent microcomb generated with various integrated nonlinear platforms.

Platform	Comb type	Q-factor (10^6)	FSR (GHz)	On-chip Power (mW)	Soliton Step (GHz)	On-chip Laser	Accessing Method
Silica[16]	Bright soliton	> 200	15	25	—	N	Power kicking
Si$_3$N$_4$[52]	Bright soliton	15	99	6.2	—	N	Frequency scanning
Si$_3$N$_4$[53]	Bright soliton	1.4^a	230	200	~1.5	N	Frequency scanning
Si$_3$N$_4$[3]	Bright soliton	16	15	30	N/A	Y	Injection locking
GaN[54]	Bright soliton	1.8	324	136	—	N	Manual frequency tuning (auxiliary laser)
LiNbO$_3$[55]	Bright soliton	~1.1^a	~200	~90	~0.5	N	Bidirectional scanning
LiNbO$_3$[56]	Bright soliton	2.2^a	199.7	33	~0.5	N	Bidirectional scanning
SiC[57]	Bright soliton	5.6	350	2.3	~0.014	N	Frequency tuning in cryostat
Hydex[58]	Soliton crystal	1.5	48.9	~1100	—	N	Manual frequency tuning
AlN[59]	Bright soliton	1.4	374	~335	10.4	N	Manual frequency tuning (auxiliary resonance)
AlN[60]	Bright soliton	1.6	433	~390	~10	N	Frequency scanning
Ta$_2$O$_5$[61]	Bright soliton	0.4^a	1000	36	~3	N	Frequency scanning
Si$_3$N$_4$[34]	Dark-pulse	5.7	104.8	2.5	~0.25	N	Frequency scanning
Si$_3$N$_4$[31]	Dark-pulse	0.77^a	231.3	~850	~37.5	N	Thermally tuned resonance
Si$_3$N$_4$[4]	Dark-pulse	260	5	~20	N/A	Y	Injection locking
Si$_3$N$_4$[62]	Dark-pulse	>10	26.2	5	N/A	Y	Injection locking
AlGaAsOI (this work)	Dark-pulse	2.36	90	<0.93 ~150	0.3 97.5 (>1 FSR)	Y	No tuning, no feedback required

^{a}Represents the loaded Q.

order of magnitude higher than that of typical bright soliton microcombs. This efficiency can be further increased by improving coupling or introducing coupled-microresonator geometry for dynamic adjustment of AMXs.[33,34,66] The high efficiency will contribute to a higher optical carrier-to-noise ratio for information carriers. Such superiority has already been demonstrated in its favor of a Pbit/s level ultradense coherent data transmission system[67] and a chip-scale IMDD data transmission system.[68] Also, with an ultrawide range microcomb tuning, the spectrum information could be acquired seamlessly by scanning the comb across the entire FSR, which will benefit high-resolution spectroscopy. The large frequency chirping capability would also raise the ranging resolution by almost 2 orders of magnitude when applied to FMCW lidar applications.

Our results represent a key milestone toward laser-integrated microcomb sources favorable for tremendous system-level applications. The compact and robust microcomb module comprising a DFB laser and the AlGaAsOI microresonator has for the first time, we believe, enabled the union of microcomb and silicon photonic engines for optoelectronic systems.[68] Moving forward, with the assistance of an on-chip isolator, chip-to-chip coupling of the laser and microresonator will further improve the integration level of the system.[1–4] It is worth noting that monolithic integration of the AlGaAsOI microresonators with III-V gain sections is feasible, given the excellent compatibility of the joint fabrication process, which is considerably simpler than the current heterogeneously integrated laser-soliton microcomb technology. Overall, the realization of ultraefficient coherent microcombs with wide tunability and operation simplicity in high-Q III-V microresonators provides a promising solution for microcomb generation, and it will accelerate the adoption of frequency comb sources in practical applications, such as lidar, data transmission, and optical neural networks.[26,63,69]

4 Appendix A: Design and Fabrication of the Devices

The pulley-type AlGaAsOI resonators were designed to be slightly overcoupled and exhibit normal dispersion within the C-band. An inverse taper with the waveguide width adiabatically narrowed to 200 nm is used here for efficient chip-to-fiber coupling; the coupling loss is ~2–3 dB/facet. The fabrication of AlGaAs microresonators was based on heterogeneous wafer bonding. The molecular-beam epitaxy growth method was employed for the AlGaAs epitaxial wafer. A 248 nm deep-ultraviolet stepper was used for the lithography. A photoresist reflow process and an optimized dry-etch process were applied in waveguide patterning for waveguide scattering loss reduction. For passivation, the core is fully clad by consecutive deposition of silica via atomic layer deposition and plasma-enhanced chemical vapor deposition. The detailed fabrication process can be found in our previous works in Refs. 29 and 30.

5 Appendix B: Experimental Details

The Q factor measurement is performed by scanning an external cavity diode laser (Toptica CTL 1550) across a resonance from the blue side to the red side. To avoid the distortion of line shape caused by thermal nonlinearity, the on-chip power is reduced to tens of microwatts. The dispersion of the resonance is obtained by scanning the laser over a larger wavelength range (from 1520 to 1630 nm) and recording the transmission spectrum. The frequency of the laser is referenced to a Mach–Zehnder interferometer, which is calibrated by a fiber comb. Considering the differences in coupling efficiency on the two sides, the lowest on-chip pump power was evaluated by recording the off-chip power of both sides, afterward subtracting the average coupling loss of the two sides. In that case, the estimated on-chip pump power of ~930 μW and ~870 W is measured; thus the actual on-chip power should be lower than 930 μW.

For RIN characterization, the RIN of a low-noise continuous-wave (CW) laser is first tested to evaluate the measurement floor, whose power nearly saturates the photodetector (Newport 1811-FC). The measurement floor at high-offset frequency is around −140 dB Hz^{-1}, which is primarily limited by the noise-equivalent-power of the photodetector. For comb-line measurement, the microcomb is generated with the temperature of the microresonator adjusted to 20.8°C. Then, a notch filter is used to attenuate the strong pump and a pair of adjacent comb lines before the comb is sent into an erbium-doped fiber amplifier (EDFA). Individual comb lines are then selected using a tunable bandpass filter, and their RIN is characterized by a phase noise analyzer (Rohde & Schwarz FSUP 26.5) using the baseband measurement function.

A delayed self-heterodyne setup is used to measure the frequency noise of the comb lines. The setup consists of a 5-km-long fiber delay line. The AOM is driven by a low-noise microwave source at 55 MHz, while the zeroth-order and first-order signals are sent into the two arms of the interferometer before they are recombined and detected. The signals are recorded using an oscilloscope (Keysight MXR404A) and are Hilbert-transformed to extract the instantaneous frequency fluctuations for computation of power spectral densities. To omit the etalon effect, for high offset frequencies (>20 kHz), the noises are plotted at certain frequencies given by $f = (2n - 1)/2\tau$, with n positive integers and τ the relative temporal delay between the two arms.

The frequency chirping of the microcomb is performed by directly modulating the pump frequency using an AFG to drive the PZT unit of the external-cavity diode laser. The pump wavelength is around 1551.1 nm, with a microresonator temperature of 16°C. The pump laser is first manually tuned into the resonance and stopped at the center of the transmission step. Then, the triangular frequency modulation of the pump laser is turned on. A wavelength-selective switch is employed to filter out each chirped comb line, which is recorded by a high-precision wavelength meter (HighFinesse WS6 Series). The period of the symmetric triangular frequency-modulation signal is set to 10 s to satisfy the measurement repetition rate of the wavelength meter, corresponding to the frequency scanning speed of 2 GHz/s. For fast chirping, a ~400 kHz FMCW pump signal is generated by an arbitrary waveform generator (Tektronix AWG70001B) with a 100 GSa/s sampling rate. The chirping comb lines are filtered out by a wavelength-selective switch (WSS) and characterized by heterodyne detection. The data are recorded by an 80 GSa/s real-time oscilloscope. Then, the instantaneous frequency is determined via short-time Fourier transform.

6 Appendix C: Numerical Simulation

To give a better insight into the self-stimulation of the dark pulse in our devices, two mode families are considered here. One mode family is the dark-pulse-supporting mode family, referred
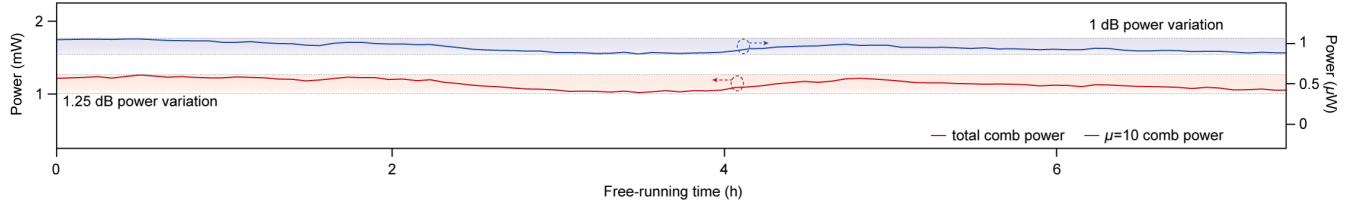
Fig. 6 Long-term stability of the microcomb. The optical spectra of the microcomb are continuously recorded for over 7 h, and the total comb power (red) and power of the 10th comb line (blue) are plotted, showing 1.25 and 1 dB variations, respectively.

to as the primary (P) mode family, and the other mode family is referred to as the auxiliary (A) mode family. The AMX between the two mode families strongly modified the local dispersion, facilitating the self-stimulation of dark pulses.[31,70] The linear coupling between the primary modes and auxiliary modes is introduced into the Lugiato-Lefever equations (LLEs),

$$t_R \frac{\partial E^{(P)}(t,\tau)}{\partial t} = \left[-(\alpha^{(P)} - it_R\delta) + iL\frac{\beta_2^{(P)}}{2}\frac{\partial^2}{\partial \tau^2} \right] E^{(P)} + iL\gamma^{(P)}|E^{(P)}|^2 E^{(P)} + iL\kappa E^{(A)} + \sqrt{\theta}E_{\text{in}}, \quad (1)$$

$$t_R \frac{\partial E^{(A)}(t,\tau)}{\partial t} = \left[-(\alpha^{(A)} - it_R\delta - i\Delta) + iL\frac{\beta_2^{(A)}}{2}\frac{\partial^2}{\partial \tau^2} \right] E^{(A)} + iL\gamma^{(A)}|E^{(A)}|^2 E^{(A)} + iL\kappa E^{(P)}. \quad (2)$$

$E^{(P)}$ and $E^{(A)}$ stand for the intracavity temporal fields in the primary and the auxiliary modes, respectively, $\alpha^{(P)} = 0.0067$ and $\alpha^{(A)} = 0.02$ are the round-trip cavity loss factor, $\beta_2^{(P)} = 139 \text{ ps}^2 \text{ km}^{-1}$ and $\beta_2^{(A)} = -2421 \text{ ps}^2 \text{ km}^{-1}$ represent the second-order dispersion coefficients, and $\delta = \omega_0^{(P)} - \omega_p$ is the detuning, where $\omega_0^{(P)}$ is the resonance frequency of the primary mode and ω_p is the frequency of the pump field. $t_R = 11.628 \text{ ps}$ is the round-trip time of the primary mode and $L = 2\pi \times 144 \text{ } \mu\text{m}$ is the round-trip length. The pump field is coupled into the primary mode by $\sqrt{\theta}E_{\text{in}}$, where $\theta = 0.0067$ is the waveguide coupling coefficient and E_{in} is the pump field. The coupling between the pump field and the auxiliary mode is ignored, due to the relatively small coupling rate in the pulley couplers. $\gamma^{(P)} = 340 \text{ m}^{-1} \text{ W}^{-1}$ and $\gamma^{(A)} = 330 \text{ m}^{-1} \text{ W}^{-1}$ are the nonlinear coefficients. The linear coupling between two mode families is induced by $iL\kappa E^{(x)}(x = A, P)$, where $\kappa = 84 \text{ m}^{-1}$ is the linear coupling strength. Δ indicates the resonant frequency difference between the two modes, which is equal to $t_R[(\omega_0^{(A)} - \omega_0^{(P)}) - i(\beta_1^{(A)} - \beta_1^{(P)})\frac{\partial}{\partial \tau}]$, where $\omega_0^{(A)}$ is the resonance frequency, and $\beta_1^{(P)} = 12.280 \text{ ns/m}$ and $\beta_1^{(A)} = 13.438 \text{ ns/m}$ are the first-order dispersion coefficients. All paramaters used for simulation can be extracted from the experiment data. The $\omega_0^{(A)} - \omega_0^{(P)}$ is tuned to simulate the change of AMX. To get the results shown in Fig. 2(b), the $t_R(\omega_0^{(A)} - \omega_0^{(P)})$ is set to 0.81. In Fig. 2(d), the $t_R(\omega_0^{(A)} - \omega_0^{(P)})$ is set to -0.01, -1.40, -1.96, and -2.49 for dark pulses with different FSRs.

7 Appendix D: Long-term Stability Measurement

The long-term stability is evaluated through real-time power recording of a free-running microcomb. The comb spectra are periodically recorded by an optical spectrum analyzer every 5 min. The power drift of the microcomb is then obtained and analyzed, as shown in Fig. 6. The total comb power varies within 1.25 dB during 7 h of operation duration and 1 dB for certain comb lines. The lasting time highly depends on the pump power drift, which is suspected to be caused by the instability of the coupling setup and the temperature variations. Such instability can be significantly suppressed once the device is optically packaged with good temperature control.

Data, Materials, and Code Availability

The data and code for numerical calculation that support the findings of this study are available from the corresponding authors upon reasonable request.

Author contributions

The experiments were conceived by H.S., L.C., and Q.-F.Y. The devices were designed by H.S., L.C., and W.X. The microcomb simulation and modelling were conducted by B.S. The AlGaAsOI microresonators were fabricated by W.X. and L.C. The dispersion and noise were measured by C.L. and Q.-F.Y. Other characterizations were conducted by H.S. and B.S, with the assistance from R.C., X.Z., M.J., Y.T., and Z.T. The results were analyzed by H.S., C.L., and B.S. All authors participated in writing the manuscript. The project was coordinated by H.S., L.C., and Q.-F.Y., under the supervision of S.Y., X.W., and J.E.B.

References

1. B. Stern et al., "Battery-operated integrated frequency comb generator," *Nature* **562**(7727), 401–405 (2018).
2. A. S. Raja et al., "Electrically pumped photonic integrated soliton microcomb," *Nat. Commun.* **10**(1), 680 (2019).
3. B. Shen et al., "Integrated turnkey soliton microcombs," *Nature* **582**(7812), 365–369 (2020).

4. W. Jin et al., "Hertz-linewidth semiconductor lasers using CMOS-ready ultra-high-Q microresonators," *Nat. Photonics* **15**(5), 346–353 (2021).

5. C. Xiang et al., "Laser soliton microcombs heterogeneously integrated on silicon," *Science* **373**(6550), 99–103 (2021).

6. T. J. Kippenberg et al., "Dissipative Kerr solitons in optical microresonators," *Science* **361**(6402), eaan8083 (2018).

7. L. Chang, S. Liu, and J. E. Bowers, "Integrated optical frequency comb technologies," *Nat. Photonics* **16**(2), 95–108 (2022).

8. S. T. Cundiff and J. Ye, "Colloquium: femtosecond optical frequency combs," *Rev. Mod. Phys.* **75**(1), 325–342 (2003).

9. S. A. Diddams, K. Vahala, and T. Udem, "Optical frequency combs: coherently uniting the electromagnetic spectrum," *Science* **369**(6501), eaay3676 (2020).

10. M.-G. Suh et al., "Microresonator soliton dual-comb spectroscopy," *Science* **354**(6312), 600–603 (2016).

11. Q.-F. Yang et al., "Vernier spectrometer using counterpropagating soliton microcombs," *Science* **363**(6430), 965–968 (2019).

12. Z. L. Newman et al., "Architecture for the photonic integration of an optical atomic clock," *Optica* **6**(5), 680–685 (2019).

13. D. T. Spencer et al., "An optical-frequency synthesizer using integrated photonics," *Nature* **557**(7703), 81–85 (2018).

14. D. T. Spencer et al., "Integrated waveguide coupled Si_3N_4 resonators in the ultrahigh-Q regime," *Optica* **5**(3), 153–157 (2014).

15. X. Ji et al., "Ultra-low-loss on-chip resonators with sub-milliwatt parametric oscillation threshold," *Optica* **4**(6), 619–624 (2017).

16. K. Y. Yang et al., "Bridging ultrahigh-Q devices and photonic circuits," *Nat. Photonics* **12**(5), 297–302 (2018).

17. J. Liu et al., "Photonic microwave generation in the X- and K-band using integrated soliton microcombs," *Nat. Photonics* **14**, 486–491 (2020).

18. K. Liu et al., "720 million quality factor integrated all-waveguide photonic resonator," in *Device Res. Conf. (DRC)*, IEEE, pp. 1–2 (2021).

19. Z. Ye et al., "High-Q Si_3N_4 microresonators based on a subtractive processing for Kerr nonlinear optics," *Opt. Express* **27**, 35719–35727 (2019).

20. Z. Ye et al., "Overcoming the quantum limit of optical amplification in monolithic waveguides," *Sci. Adv.* **7**(38), eabi8150 (2021).

21. X. Yi et al., "Active capture and stabilization of temporal solitons in microresonators," *Opt. Lett.* **41**(9), 2037–2040 (2016).

22. H. Zhou et al., "Soliton bursts and deterministic dissipative Kerr soliton generation in auxiliary-assisted microcavities," *Light Sci. Appl.* **8**(1), 50 (2019).

23. J. Liu et al., "High-yield, wafer-scale fabrication of ultralow-loss, dispersion-engineered silicon nitride photonic circuits," *Nat. Commun.* **12**(1), 2236 (2021).

24. T. Herr et al., "Temporal solitons in optical microresonators," *Nat. Photonics* **8**(2), 145–152 (2014).

25. J. R. Stone et al., "Thermal and nonlinear dissipative-soliton dynamics in Kerr-microresonator frequency combs," *Phys. Rev. Lett.* **121**(6), 063902 (2018).

26. J. Riemensberger et al., "Massively parallel coherent laser ranging using a soliton microcomb," *Nature* **581**(7807), 164–170 (2020).

27. T. Lin et al., "Broadband ultrahigh-resolution chip-scale scanning soliton dual-comb spectroscopy," arXiv:2001.00869 (2020).

28. M. Gao et al., "Probing material absorption and optical nonlinearity of integrated photonic materials," *Nat. Commun.* **13**(1), 3323 (2022).

29. L. Chang et al., "Ultra-efficient frequency comb generation in AlGaAs-on-insulator microresonators," *Nat. Commun.* **11**(1), 1331 (2020).

30. W. Xie et al., "Ultrahigh-Q AlGaAs-on-insulator microresonators for integrated nonlinear photonics," *Opt. Express* **28**(22), 32894–32906 (2020).

31. X. Xue et al., "Mode-locked dark pulse Kerr combs in normal-dispersion microresonators," *Nat. Photonics* **9**(9), 594–600 (2015).

32. V. Lobanov et al., "Frequency combs and platicons in optical microresonators with normal GVD," *Opt. Express* **23**(6), 7713–7721 (2015).

33. B. Y. Kim et al., "Turn-key, high-efficiency Kerr comb source," *Opt. Lett.* **44**(18), 4475–4478 (2019).

34. Ó. B. Helgason et al., "Dissipative solitons in photonic molecules," *Nat. Photonics* **15**(4), 305–310 (2021).

35. Y. Guo et al., "Thermally tuned high-performance III-V/Si_3N_4 external cavity laser," *IEEE Photonics J.* **13**(2), 1500813 (2021).

36. E. Nazemosadat et al., "Switching dynamics of dark-pulse Kerr frequency comb states in optical microresonators," *Phys. Rev. A* **103**, 013513 (2021).

37. X. Yi et al., "Soliton frequency comb at microwave rates in a high-Q silica microresonator," *Optica* **2**(12), 1078–1085 (2015).

38. V. Brasch et al., "Photonic chip-based optical frequency comb using soliton Cherenkov radiation," *Science* **351**(6271), 357–360 (2016).

39. G. Moille et al., "Kerr-microresonator soliton frequency combs at cryogenic temperatures," *Phys. Rev. Appl.* **12**(3), 034057 (2019).

40. G. Moille et al., "Dissipative Kerr solitons in a III-V microresonator," *Laser Photonics Rev.* **14**(8), 2000022 (2020).

41. D. C. Cole et al., "Soliton crystals in Kerr resonators," *Nat. Photonics* **11**(10), 671–676 (2017).

42. M. Karpov et al., "Dynamics of soliton crystals in optical microresonators," *Nat. Phys.* **15**(10), 1071–1077 (2019).

43. Z. Lu et al., "Synthesized soliton crystals," *Nat. Commun.* **12**(1), 3179 (2021).

44. J. Hu et al., "Reconfigurable radiofrequency filters based on versatile soliton microcombs," *Nat. Commun.* **11**(1), 4377 (2020).

45. B. Wang et al., "Towards high-power, high-coherence, integrated photonic mmWave platform with microcavity solitons," *Light Sci. Appl.* **10**(1), 4 (2021).

46. M. Pu et al., "Efficient frequency comb generation in AlGaAs-on-insulator," *Optica* **3**(8), 823–826 (2016).

47. P. A. Roos et al., "Ultrabroadband optical chirp linearization for precision metrology applications," *Opt. Lett.* **34**(23), 3692–3694 (2009).

48. D. Uttam and B. Culshaw, "Precision time domain reflectometry in optical fiber systems using a frequency modulated continuous wave ranging technique," *J. Lightwave Technol.* **3**(5), 971–977 (1985).

49. M. Karpov et al., "Raman self-frequency shift of dissipative Kerr solitons in an optical microresonator," *Phys. Rev. Lett.* **116**, 103902 (2016).

50. A. V. Cherenkov, V. E. Lobanov, and M. L. Gorodetsky, "Dissipative Kerr solitons and Cherenkov radiation in optical microresonators with third-order dispersion," *Phys. Rev. A* **95**, 033810 (2017).

51. X. Yi et al., "Single-mode dispersive waves and soliton microcomb dynamics," *Nat. Commun.* **8**(1), 14869 (2017).

52. J. Liu et al., "Ultralow-power chip-based soliton microcombs for photonic integration," *Optica* **5**, 1347–1353 (2018).

53. Q. Li et al., "Stably accessing octave-spanning microresonator frequency combs in the soliton regime," *Optica* **4**(2), 193–203 (2017).

54. Y. Zheng et al., "Integrated gallium nitride nonlinear photonics," *Laser Photonics Rev.* **16**(1), 2100071 (2022).

55. Z. Gong et al., "Soliton microcomb generation at 2 μm in z-cut lithium niobate microring resonators," *Opt. Lett.* **44**, 3182–3185 (2019).

56. Y. He et al., "Self-starting bi-chromatic $LiNbO_3$ soliton microcomb," *Optica* **6**, 1138–1144 (2019).

57. M. A. Guidry et al., "Quantum optics of soliton microcombs," *Nat. Photonics* **16**(1), 52–58 (2022).

58. M. Tan et al., "Photonic RF arbitrary waveform generator based on a soliton crystal micro-comb source," *J. Lightwave Technol.* **38**(22), 6221–6226 (2020).

59. H. Weng et al., "Directly accessing octave-spanning dissipative Kerr soliton frequency combs in an AlN microresonator," *Photonics Res.* **9**, 1351–1357 (2021).
60. X. Liu et al., "Aluminum nitride nanophotonics for beyond-octave soliton microcomb generation and self-referencing," *Nat. Commun.* **12**(1), 5428 (2021).
61. S.-P. Yu et al., "Spontaneous pulse formation in edgeless photonic crystal resonators," *Nat. Photonics* **15**(6), 461–467 (2021).
62. G. Lihachev et al., "Platicon microcomb generation using laser self-injection locking," *Nat. Commun.* **13**(1), 1771 (2022).
63. B. Corcoran et al., "Ultra-dense optical data transmission over standard fibre with a single chip source," *Nat. Commun.* **11**(1), 2568 (2020).
64. X. Xu et al., "11 TOPS photonic convolutional accelerator for optical neural networks," *Nature* **589**(7840), 44–51 (2021).
65. X. Xu et al., "Microcomb-based photonic RF signal processing," *IEEE Photonics Technol. Lett.* **31**(23), 1854–1857 (2019).
66. X. Xue et al., "Normal-dispersion microcombs enabled by controllable mode interactions," *Laser Photonics Rev.* **9**(4), L23–L28 (2015).
67. A. Jørgensen et al., "Petabit-per-second data transmission using a chip-scale microcomb ring resonator source," *Nat. Photonics* **16**, 798–802 (2022).
68. H. Shu et al., "Microcomb-driven silicon photonic systems," *Nature* **605**(7910), 457–463 (2022).
69. J. Feldmann et al., "Parallel convolutional processing using an integrated photonic tensor core," *Nature* **589**(7840), 52–58 (2021).
70. Y. Liu et al., "Investigation of mode coupling in normal-dispersion silicon nitride microresonators for Kerr frequency comb generation," *Optica* **5**(3), 137–144 (2014).

Haowen Shu received his BS degree in electrical engineering from Beijing University of Posts and Telecommunications in 2015 and his PhD from Peking University in 2020. He is currently an assistant professor at Peking University. His research interests lie in silicon photonics and its system-level applications.

Lin Chang is an assistant professor at Peking University. He received his PhD in photonics from the University of California, Santa Barbara. His research focus is integrated photonics, particularly heterogeneous silicon photonics. He has demonstrated fully integrated microcomb and ultra-narrow-linewidth laser on chip, benefiting applications from communications to LiDAR. He is the author of more than 40 papers. He is the recipient of "2022 Rising Stars of Light" and "2023 IEEE Photonic Society Young Investigator Award."

Chenghao Lao is a PhD candidate at Peking University. He received his BS degree in physics from Huazhong University of Science and Technology in 2018. His current research interests include integrated photonics, microcombs, and semiconductor laser.

Bitao Shen is a PhD student at the Peking University. He received his BS degree of engineering degree from Xidian University in 2019. His current research interests include nonlinear optics, integrated photonics, and optoelectronic systems.

Weiqiang Xie is an associate professor at Shanghai Jiao Tong University. He received his bachelor's degree from Xi'an Jiaotong University in 2008 and his master's degree from Shanghai Jiao Tong University in 2011. He received his PhD in photonics engineering at Ghent University in 2016. His current research focuses on silicon/silicon nitride/III-V photonic integrated circuits and their heterogeneous integration with other materials for various applications. He has authored and coauthored over 70 journal papers.

Shaohua Yu is a member of the Chinese Academy of Engineering, with the research focusing on fiber optic communications. He is also an adjunct professor at Peking University. He is recipient of a number of awards: the second prize of the National Technology Invention Award and the second prize of the National Science and Technology Progress Award.

Qifan Yang is an assistant professor at Peking University. He received his BSc degree in physics from Peking University in 2013 and his PhD in applied physics from California Institute of Technology in 2019. He is the author of more than 30 journal papers. His current research interests include integrated photonics and nonlinear optics, especially optical microresonators and frequency combs.

Xingjun Wang is a full professor at Peking University. He received his BE, ME, and PhD degrees from Dalian University of Technology. He is the author of more than 110 journal papers and has received 28 patents. His research interests focus on integrated photonic devices and on-chip optoelectronic systems, especially for optical communications, optical neural networks and lidar.

John E. Bowers holds the Fred Kavli Chair in Nanotechnology and is the Director of the Institute for Energy Efficiency and a distinguished professor in the Department of Electrical and Computer Engineering at UC Santa Barbara. He received his MS and PhD degrees from Stanford University. His research focus is silicon photonics and optical communications. He has published two books, 450 journal papers, 1000 conference papers, and has received 54 patents.

Biographies of the other authors are not available.